



HAL
open science

On the Migration of a High-Angle Grain Boundary-Effect of Shear Stress and Energy Jump-Driving Force on Micro-Bicrystals

Jorge Rafael Velayarce, Xiaolei Chen, Stéphane Berbenni, Christian Motz

► **To cite this version:**

Jorge Rafael Velayarce, Xiaolei Chen, Stéphane Berbenni, Christian Motz. On the Migration of a High-Angle Grain Boundary-Effect of Shear Stress and Energy Jump-Driving Force on Micro-Bicrystals. *Advanced Engineering Materials*, 2024, 26 (19), pp.2400406. 10.1002/adem.202400406 . hal-04660521

HAL Id: hal-04660521

<https://hal.univ-lorraine.fr/hal-04660521v1>

Submitted on 17 Nov 2024

HAL is a multi-disciplinary open access archive for the deposit and dissemination of scientific research documents, whether they are published or not. The documents may come from teaching and research institutions in France or abroad, or from public or private research centers.

L'archive ouverte pluridisciplinaire **HAL**, est destinée au dépôt et à la diffusion de documents scientifiques de niveau recherche, publiés ou non, émanant des établissements d'enseignement et de recherche français ou étrangers, des laboratoires publics ou privés.



Distributed under a Creative Commons Attribution - NonCommercial - NoDerivatives 4.0
International License

On the Migration of a High-Angle Grain Boundary—Effect of Shear Stress and Energy Jump-Driving Force on Micro-Bicrystals

Jorge Rafael Velayarce,* Xiaolei Chen, Stéphane Berbenni, and Christian Motz

Grain boundary (GB) migration plays a crucial role in the microstructural evolution of polycrystalline materials, particularly in fine-grained materials. This migration can be driven by shear forces or by an energy jump across a GB. Interestingly, GB migration processes during cyclic loading deformations have been observed to be fully reversible. This study focuses on understanding the impact and importance of shear driving forces, the free energy difference across a GB, and lattice dislocations on GB migration. These factors are key points for gaining deeper insights into the underlying mechanisms of GB migration. In this work, GB migration in cyclic loading deformations is demonstrated, and it is emphasized that it clearly depends on both the shear driving forces (attributed to the motion of disconnections) and the energy differential across the GB. Two cyclic micro-experimental methods, accompanied by analytical and numerical simulations, have been employed to investigate the role of shear stresses and energy jump-driving forces in GB migration. This investigation provides clear experimental evidence that GB migration, in particular for a high-angle GB, is dependent on both stress and energy driving forces.

1. Introduction

The most important properties of crystalline materials are controlled or, at least, strongly influenced by the presence of grain boundaries (GBs) and lattice dislocations. For example, GBs are known to interact with lattice dislocations, acting as strong obstacles to free dislocation motion. Consequently, the GB density in polycrystalline materials significantly impacts


the material properties, such as strength, ductility, fracture, toughness, and fatigue strength, due to elastic and plastic anisotropies.^[1–3]

In fine-grained materials, GB-based plasticity mechanisms, such as GB migration, sliding, and grain rotation, have been revealed to be fundamental for the mechanical behavior of such fine-grained materials.^[4–8] Among all the GB-based plasticity mechanisms, the shear-coupled GB migration has been the subject of both theoretical^[9–11] and experimental studies.^[12–15] Stress-induced GB migration was first discovered experimentally in the 1950s for low-angle GBs (LAGB).^[16] For LAGB, stress-induced GB migration was interpreted in terms of collective motion of single intrinsic dislocations.^[17] In addition, high-angle GBs (HAGBs) were also seen to move under applied stress.^[18]

More recently, many experimental data confirmed this stress-induced GB mechanism for high-purity planar Al bicrystals with both [001] tilt LAGB and HAGB (from 0 to 90° misorientations).^[19–23] By performing mechanical tests on Al bicrystals on a wide range of temperature (from 280 to 400 °C), Gorkaya et al.^[22] showed that GB migration is a thermally activated process and there is a misorientation dependence of activation parameters like activation enthalpy and mobility pre-exponential factor. The mechanism of stress-induced shear-coupled GB migration at room temperature is today well identified by a shear deformation accompanying GB migration for symmetric (coincident) tilt GB (here denoted STGB) but less for general nonsymmetric GB. This new deformation mechanism is different from strain-induced GB migration studied for recrystallization phenomena. The ratio between this shear displacement parallel to the GB plane and the normal displacement owing to GB motion was introduced as the “ β ” shear coupling factor, which depends on intrinsic GB defects; see^[9–11] details. Molecular dynamics (MD) simulations^[10,24–27] and experimental investigations^[28–30] have revealed that the microscopic mechanisms involved in GB migration are associated with the nucleation and motion of intrinsic GB dislocations (GBDs) along the GB. These defects are also called disconnections, which are defined as interfacial line defects with both dislocation and step character, as proposed by Ashby^[31] and Hirth et al.^[32–34] In fine-grained metals deformed under static loading conditions, stress-assisted GB migration, manifesting as grain growth, has been

J. R. Velayarce, X. Chen, C. Motz
Institute of Material Science and Methods
Saarland University
Saarbrücken D-66123, Germany
E-mail: r.velayarce@matsci.uni-sb.de

X. Chen, S. Berbenni
Université de Lorraine, CNRS, Arts et Métiers ParisTech, LEM3
F-57000 Metz, France

 The ORCID identification number(s) for the author(s) of this article can be found under <https://doi.org/10.1002/adem.202400406>.

© 2024 The Author(s). Advanced Engineering Materials published by Wiley-VCH GmbH. This is an open access article under the terms of the Creative Commons Attribution-NonCommercial-NoDerivs License, which permits use and distribution in any medium, provided the original work is properly cited, the use is non-commercial and no modifications or adaptations are made.

DOI: 10.1002/adem.202400406

proven to provide convincing evidences.^[5–8] For example, Gianola et al.^[6] demonstrated that Al nanograins grow much faster right around the crack tip than other grains in the material showing a hint that GBs are not static and that the enhanced ductility correlates with the stress-induced GB migration and grain growth. Therefore, stress-induced GB migration, in addition to GB sliding, has been evidenced as a dominant plasticity mechanism in small-grained materials, especially in ultrafine-grained (UFG) and nanocrystalline (NC) materials.^[6–8] These structural instabilities (GB migration) are not desirable in practical applications. Therefore, Kapp et al.^[35] emphasize that understanding the main driving forces, nature, and evolution of these structural instabilities during cyclic deformation^[36–38] will aid in developing structured materials with desired properties.

To understand the question whether GB migration is stress-induced^[7,39] or strain-induced,^[40] NC Al films have been investigated.^[7,41] The conclusion was that GB migration is driven preferentially by stress. However, other investigations have shown strain-induced GB migration during in situ nanoindentation of polycrystalline Al,^[40] uniaxial deformation of NC, Ni, and Cu,^[41] and Al bicrystals.^[42,43] More recently, GB migration has also been observed during cyclic pressure torsion of UFG Ni.^[35] However, in polycrystalline films, free surface effects and long-range interactions between grains add to the external applied one. Additionally, the curvature of GBs leads to increased wall energy. In addition to the GB pinning by, e.g., triple junctions, the GB character which continuously changes with location in curved GBs will also have contributions to the GB migration behavior.^[44] Therefore, studying planar GBs offers the advantage that the GB structure is unambiguously defined (i.e., curvature driving forces can be neglected).

Thus, the question that arises is the following: How do the loading condition (shear and normal stresses and strains) and the free energy jump across the GB do influence the (local) GB deformation/migration of a nonsymmetric GB? Currently, there is a lack of in situ experimental evidence regarding the effect of strain and shear stresses on the GB deformation/migration of HAGBs, which due to their mobility and high self-energy are a key component in the evolution of polycrystalline microstructures.^[43]

The purpose of the present work is to investigate the influence of loading conditions and slip incompatibility of the main interacting slip systems, in a particular HAGB with highly geometric GB resistance to slip transfer. Additionally, we investigate the effect of stresses arising from elastic anisotropy on GB-based deformation mechanisms, including GB damage and GB migration during in situ cyclic deformation. Our research objective was achieved through the use of scanning electron microscopy (SEM), atomic force microscopy (AFM), backscattered electron (BSE) imaging, and electron backscattered diffraction (EBSD). Our present experimental study, accompanied with analytical/numerical simulations, highlights the significance of shear stresses in GB migration mechanisms. To investigate the dependence of GB-based deformation mechanisms on the loading condition, we cyclically deformed bicrystalline microsamples under tension/compression and bending. Specifically, we developed a new testing geometry for cyclic tension/compression, in which

the applied load is parallel to the GB. This geometry ensures nearly uniform stress and strain states within the tested sample. This newly developed geometry allows for thousands of loading cycles on the bicrystal and offers advantages in terms of fabrication, gripping, and alignment of small samples compared to other methods.^[45–47] In addition, we used the cyclic bending method, which also enables the induction of many thousands of loading cycles on microbeams.^[48,49] This approach allows us to study the specific characteristics of shear-coupled GB migration.

2. Experimental Section

2.1. Sample Preparation and Characterization

Cu material with a purity of 99.99% was used for our investigation. The sample preparation methodology and heat treatment for the polycrystalline Cu sample were detailed in a previous study.^[49] The local orientation of the electropolished macrosample surface was characterized by EBSD method performed in a Carl Zeiss SIGMA series scanning electron microscope (SEM). After the crystallographic characterization of the Cu macrosample, we selected a HAGB ($\theta_{\text{miso}} = 25^\circ$) for the fabrication of the bicrystalline microsamples. This particular HAGB with tilt and twist components had a geometric GB resistance to slip transmission of $\approx 90\%$ (calculated using the STRONG method^[50]). The loading axis of the component crystals CI and CII in the standard stereographic triangle are shown in **Figure 1A**. The average Euler–Bunge angles for the two component crystals were as follows: CI ($118.9^\circ, 36.6^\circ, 0.3^\circ$) and CII ($166.8^\circ, 27^\circ, 48.2^\circ$) (in Bunge notation: (ϕ_1, ϕ, ϕ_2)).

The concept of the new geometry for cyclic tension/compression in **Figure 1A** was inspired by the cyclic bending method.^[48,49] It takes advantage of the fact that the supporting beam deforms elastically for a certain displacement in the x_1 -direction (indicated by the red arrow) over a sufficient length (L), while the test sample (bicrystal) undergoes plastic deformation. To perform this experiment, we prepared the selected GB very close to the edge of the Cu plate to facilitate the gripper placement. The sample preparation was realized using an ion milling system IM4000 from Hitachi High-Technologies. The schematic illustration in **Figure 1A** shows an overview of our new geometry for cyclic tension/compression and bending as well as SEM images of the fabricated bicrystals. The microsamples were fabricated along the x_1 -direction using the focused ion beam (FIB) technique (FEI Versa 3D FIB microscope). During fabrication, we used currents of 15 nA for rough cutting and 100–500 pA at 30 kV for fine polishing. The investigated samples had varying widths (w), ranging from ≈ 2 and 6 μm . The aspect ratio ($l:w$), which represents the ratio between the moment arm length (l) and the beam width (w), was $\approx 4:1$ for the bending beams. While the aspect ratio for the tension/compression samples was $\approx 3:1$. To reduce stress concentrations at the corners of the microsample (where the moment in bending is maximum), all microsamples were fabricated with a radius. For details, the SEM are provided in **Figure 1**.

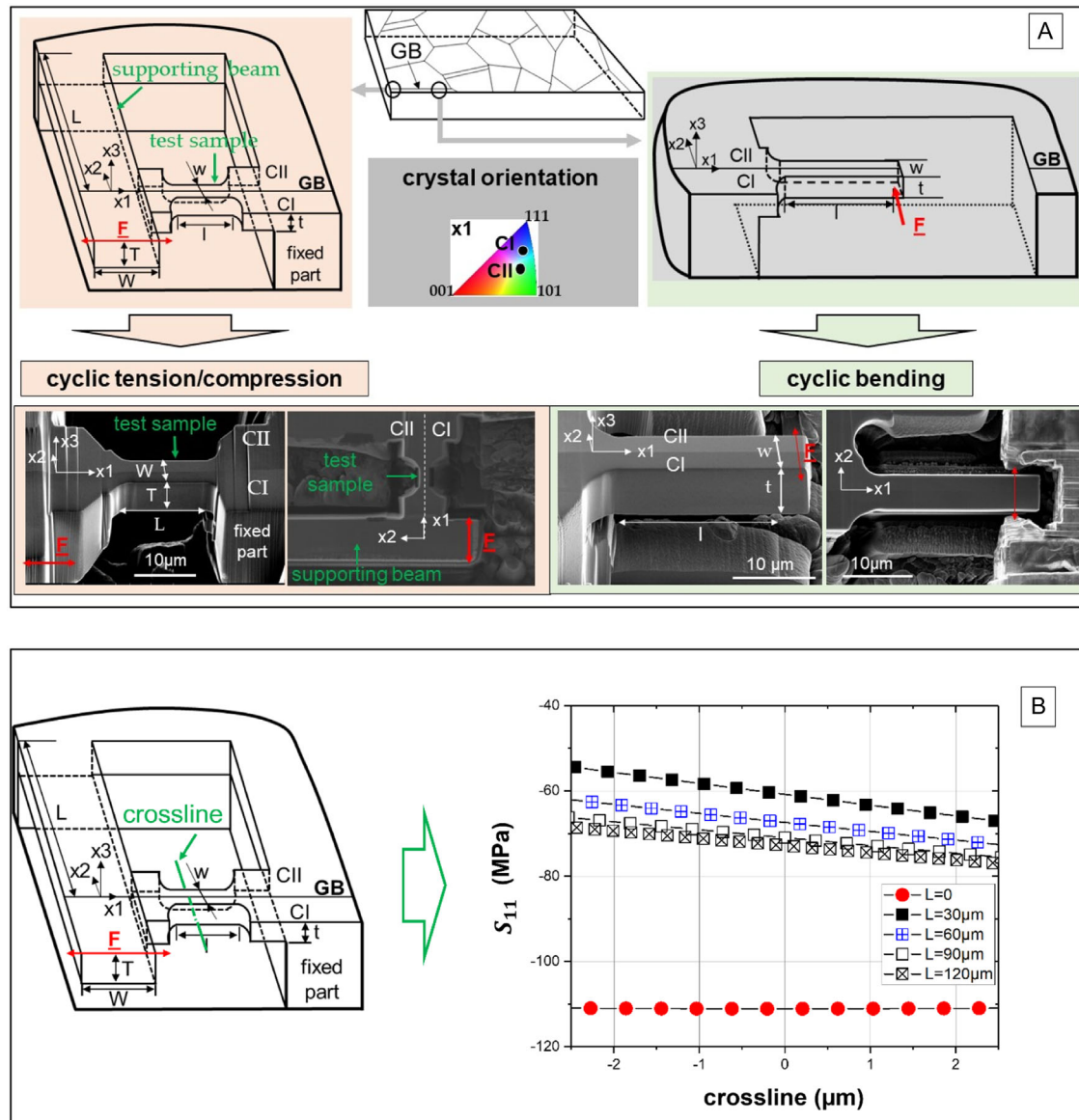


Figure 1. Schematic illustration of two setups for fatigue deformation of micro-bicrystals: A) deformation under cyclic tension/compression and cyclic bending of a bicrystal inside a SEM as well as the crystal orientation of the component crystals and B) S_{11} stresses along the crossline in the test sample in the new geometry for cyclic tension/compression tests.

2.2. FEM Simulations of the Sample Geometry for Cyclic Tension/Compression Testing

To optimize the length L of the supporting beam, which influences the S_{11} stresses on the test sample, we performed a finite element method (FEM) simulation considering the component crystals orientations of the new sample geometry. Figure 1B shows the results for the S_{11} stress in the test sample along the green crossline for different lengths L of the supporting beam ($L = 30, 60, 90,$ and $120\mu\text{m}$). As a reference, we also simulated a compression test for the same test sample geometry without supporting beam (results shown for $L = 0\mu\text{m}$). While the S_{11} results for our new geometry may

not be constant along the crossline (unlike $L = 0\mu\text{m}$), they clearly show the satisfactory elimination of the stress gradient, effectively suppressing the shear stresses existing during bending at the GB plane. Based on these FEM results, we fabricated the supporting beam with a length of $L > 60\mu\text{m}$ and a width of $W \approx 15\mu\text{m}$.

2.3. In Situ Fatigue Testing in a SEM

The fatigue tests were carried out in high vacuum environment at room temperature in a SEM equipped with an in situ nano-indenter (UNAT-SEM II). The microbeams were fatigued under full load reversal. Grippers made of polycrystalline tungsten

carbide (WC) were employed. The bicrystals were cyclically loaded with a frequency of 1 Hz, stress ratio $R = -1$, and a plastic strain amplitude ($\Delta\epsilon_p$) of $\approx 10^{-2}$. Following the fatigue testing, we analyzed the fatigue damage morphologies of all microbeams using both SEM and AFM. Subsequently, we removed the fatigue damage layer from the beam surface ($\approx 0.6\text{--}1\ \mu\text{m}$) to characterize the dislocation structures and the GB deformation using BSE imaging. The polishing of the surface roughening was performed using ion beam currents from 1 to 0.1 nA at 30 and 5 kV.

3. Results

3.1. Deformation Patterns Under Cyclic Tension/Compression Deformation

Figure 2 shows SEM, AFM, and BSE images of a bicrystal before and after the deformation using the tension/compression testing approach showed in Figure 1. In Figure 2A, the SEM image demonstrates the surface of a bicrystal with a thickness of

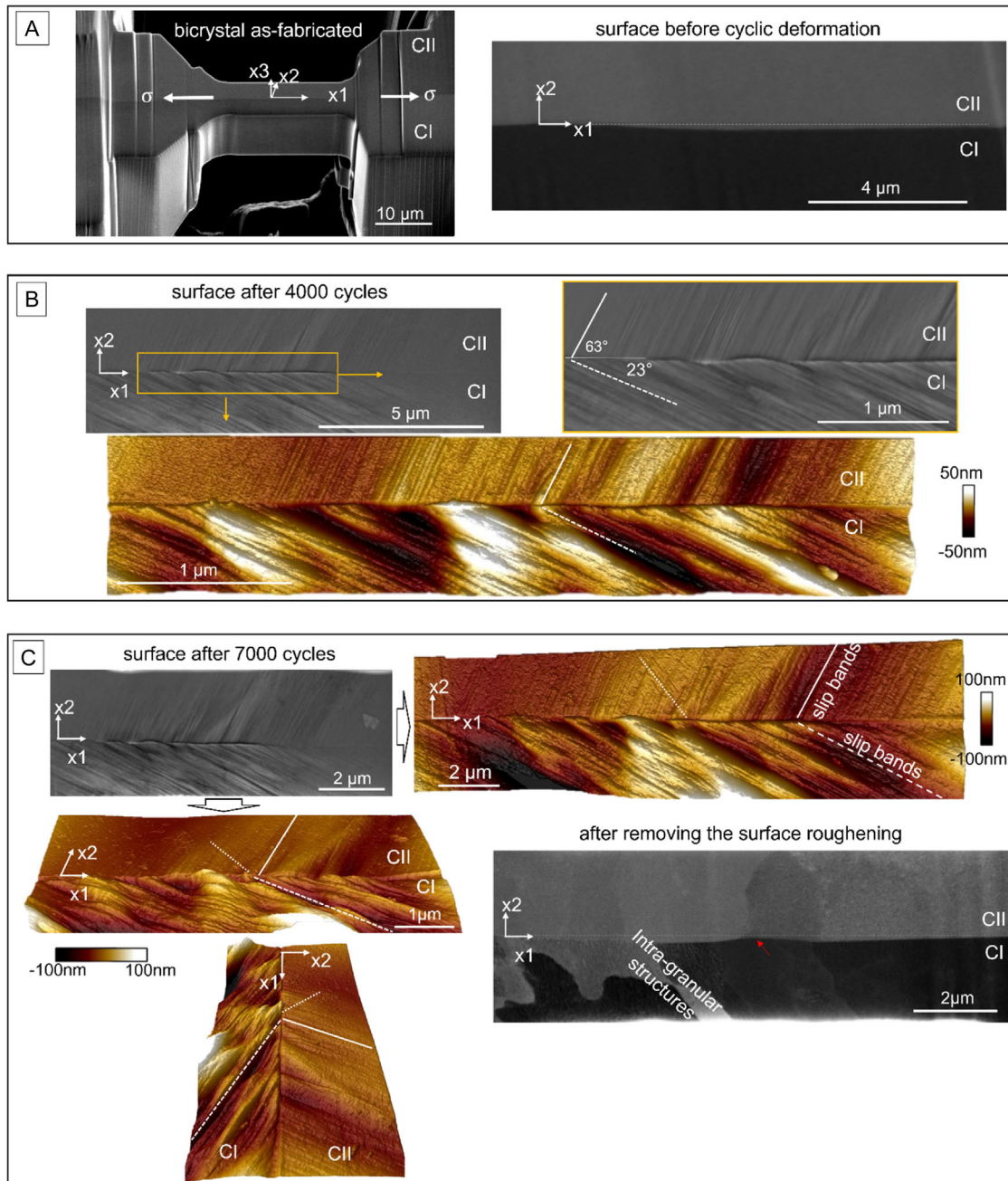


Figure 2. Cyclic deformation of a Cu bicrystal under tension/compression. A) SEM images of a micro-bicrystal before cyclic deformation. B) and C) SEM and AFM images after 4000 and 7000 cycles, respectively. These images reveal slip bands–GB interaction and slip band blockage at GB. Notably, (C) provides clearer evidence of GB damages with cycling increasing. (C) BSE image shows intragranular structures formed after 7000 cycles.

$\approx 5 \mu\text{m}$ before cyclic deformation. For later details, it should be noted here that the GB of this sample has a very slight curvature (see straight line as reference). Figure 2B,C show the slip morphologies after 4000 and 7000 cycles, respectively. As we clearly see in Figure 2B after 4000 cycles, only primary slip systems are observed and most of the primary slip bands (SBs) end at the GB. The results in Figure 2B,C also clearly show a difference of slip pattern of the two crystal components. It means that the deformed areas on the surfaces of each component grain are not compatible due to the presence of the GB as argued in.^[49] This leads to the fact that the primary SBs on CI are denser than on CII (see AFM images). However, after 7000 cycles, the AFM images in Figure 2C shows additional slip traces (dotted line) in the vicinity of the GB. Additionally, after 7000 cycles, not only increases the fatigue surface roughness in CI but also the slip step heights at the GB due to the blockage of SBs at GB. These local fatigue damages are depicted clearer in the 3D AFM images in Figure 2C.

To analyze the intragranular structures formed near the GB after fatigue, we polished the surface in the x_1 - x_2 plane using the FIB and a protecting Pt layer to avoid curtaining effect. Following this procedure, we examined the intragranular structures after 7000 cycles by BSE imaging (see Figure 2C). Clearly, the GB has a locally slight curvature because of the SBs-GB interaction in CI. This is indicated by the red arrow in the BSE image. The intragranular structures in CI are mainly aligned along the primary SBs, while in the CII the intragranular sub-boundaries are aligned almost perpendicular to the GB. These structures in CII resemble those previously reported in reference.^[49] Their formation and their sample size dependence were discussed in detail in that study. In addition, we can also recognize that there is no continuity of dislocation structures spanning the entire GB, which correlate with the intragranular of SBs at the GB. The only slight continuity of the dislocation structures is localized and correlates with the slight GB movement in the positive x_2 -direction (as indicated by the red arrow in Figure 2C).

3.2. Deformation Patterns Under Cyclic Bending Deformation

Figure 3A shows the results of the bicrystal with a thickness of $\approx 6 \mu\text{m}$ after 7000 cycles deformed using the cyclic bending method. Like the results in Figure 2, the SBs are concentrated along the primary SBs. Figure 3A also shows that the SBs density in CI is more pronounced than in CII, as observed in Figure 2. In comparison with the bicrystal in Figure 2, no secondary slip systems were activated in the vicinity of the GB. However, near to the beam surface, where larger stresses exist in bending, some additional slip lines (dash-dotted line) were observed.

Another main feature in comparison with the results in Figure 2 is the GB roughening. It appears that the GB has undergone “GB-like migration” not only at the points where the SBs intersect the GB but also along the almost its entire length. The AFM micrographs clearly show this GB-like migration mechanism. To analyze the dislocation structures in the vicinity of the GB and assess whether the GB has shifted from its original position or shows other differences compared to the results in Figure 2, we polished the surface and imaged it using the

BSE detector. The BSE images in Figure 3A demonstrates that the GB after cyclic bending deformation has slightly changed its original position (indicated by the dotted line). In comparison with the bicrystal deformed under tension/compression, the GB under cyclic bending migrated in the negative x_2 -direction, resulting in significant curvature along a large part of the GB (as shown in Figure 3A). In order to have a deeper insight into this GB migration phenomenon, smaller beams were also investigated where higher stresses exist in comparison with the larger bicrystals. These results, presented in Figure 3B, demonstrate similar GB migration features in the $6 \mu\text{m}$ bicrystal. Notably, the smaller bicrystal with a thickness of $\approx 2 \mu\text{m}$ showed significantly more GB migration after 6000 cycles than the larger one. Hence, GB migration in the smaller bicrystal was more evident than the larger one. Furthermore, a further bicrystal with a thickness of $\approx 3 \mu\text{m}$ was loaded up to 10^4 cycles using the same strain amplitude as the previous samples (Figure 3C). These results (SE, BSE, and EBSD images) provide clear confirmation of the observed GB migration. Additionally, a local crystal rotation occurs at the intersection of SBs with the GB (see red arrow on the EBSD map). Interestingly, as the sample size decreases, we observed inhomogeneities in terms of slip patterns of the crystal components CI and CII. These inhomogeneities likely arise from surface effects due to dislocation image forces^[51] (see SBs ending at some distance from the GB). These inhomogeneities can also be clearly seen in the different deformation structures in the individual component crystals.

4. Discussion

During deformation, GBs act as obstacles to the free dislocation motion and also as sources for various relaxation mechanisms.^[1] As a result, GBs significantly interrupt the dislocation motion during plastic deformation, leading to dislocation pile-ups at the GB. These pile-ups subsequently result in large local stress and strain concentrations.^[43,52–54]

In Figure 2 and 3, we observed clear differences at the GB when the bicrystals were deformed under cyclic tension/compression and cyclic bending. While the heterogeneity of plastic slip in each crystal component is likely associated with incompatibility stresses (ISs), as individual crystals in bicrystals or polycrystals tend generally to undergo different plastic strains due to the different local stresses and activated slip systems.^[1] These variations or heterogeneities also correlate with different local strain amplitudes, as stated by Nellesen et al.^[55] (see Figure 2C and 3). The results clearly showed that the GB becomes a strong barrier for primary SBs, both during cyclic tension/compression and bending (Figure 2 and 3). The results also revealed that extrusions at the GB formed over an increasing number of cycles, specifically in the samples subjected to cyclic tension/compression. These extrusions primarily result from pile-ups of mainly primary SBs. With increasing cycles, the observed extrusions become more pronounced. Consequently, intergranular-like cavitation or crack nucleation occurs at the interface between SBs and GB, as observed in uniaxial deformation of macro bi- and polycrystals.^[52,56–59] Interestingly, the samples subjected to cyclic bending do not show GB damage as the samples under tension/compression; instead, they showed GB

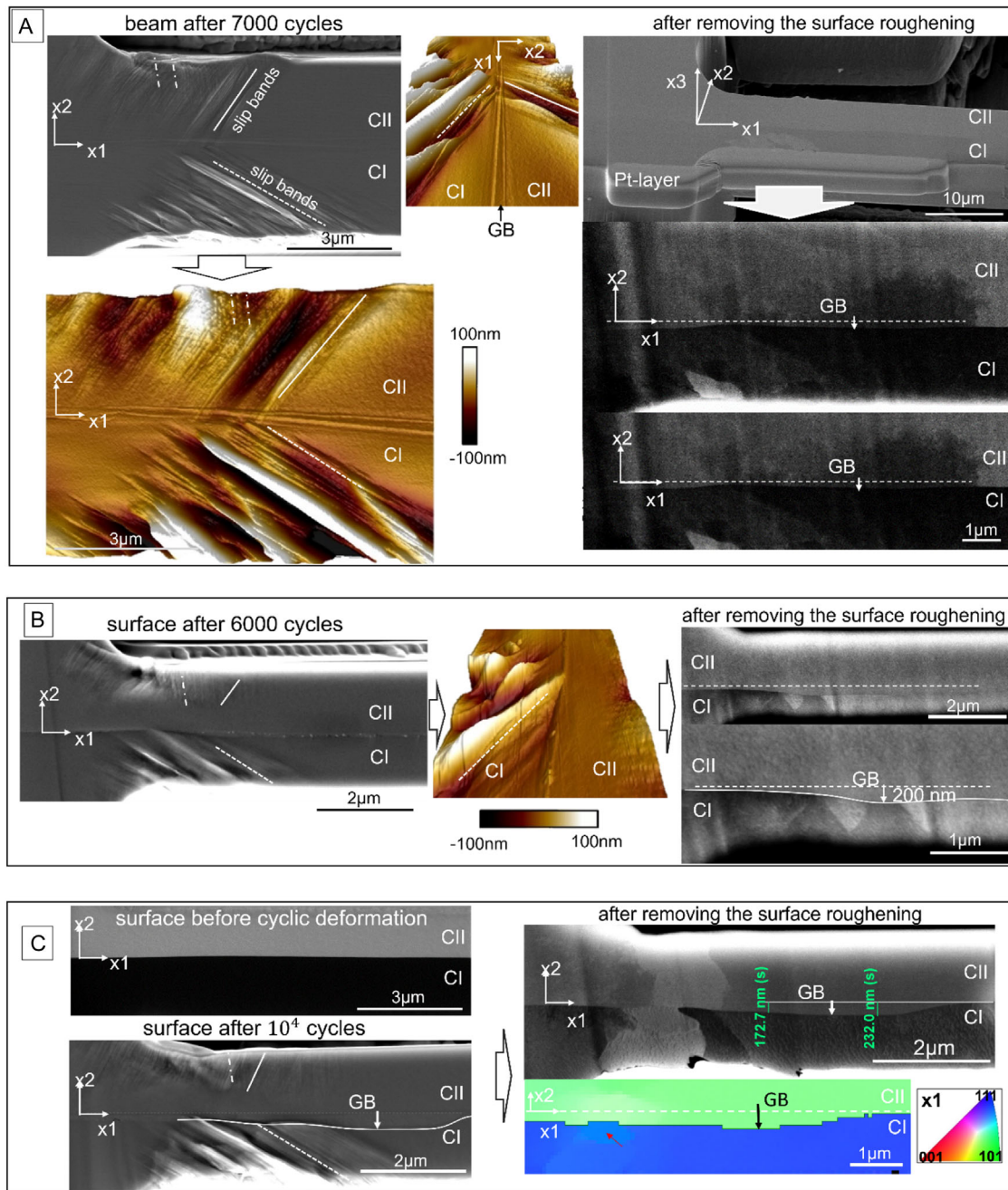


Figure 3. Cyclic deformation of a Cu bicrystal under cyclic bending. A) SEM and AFM images of a micro-bicrystal with a thickness of $\approx 6 \mu\text{m}$ after 7000 cycles. B) SEM, AFM, and BSE images of a micro-bicrystal with a thickness of $\approx 2 \mu\text{m}$ after 6000 cycles, and C) SEM, BSE, and EBSD images of a bicrystal with a thickness of $\approx 3 \mu\text{m}$ after 10^4 cycles.

migration features, which will be discussed later. During plastic deformation (whether cyclic or monotonic), interactions between SBs and GBs can often result in different dislocation mechanisms. These mechanisms include dislocation piling-up, passing through, or partially passing through at the GB. Residual dislocations within the GB (referred to GBDs) often result from these interactions. The dominant mechanism depends heavily on several factors: the type of lattice dislocations involved,^[57] the stress

state acting in or around the GB, the GB structure and character, and the degree to which the system can relax the local stress concentrations.^[1] For further insights, a review on slip transmission criteria is provided by Bayerschen et al.^[60] Based on Sangid et al.^[61] the GB energy barrier associated with SB–GB interactions is directly proportional to the magnitude of the residual Burgers vector. This means that during cyclic deformation, where the density of residual GBDs continuously increases,

the GB resistance also significantly increases. Consequently, dislocation pile-ups occur, influencing the strain incompatibility, as discussed by Li et al.^[52] By analyzing the residual GBDs based on the geometric slip transfer mechanisms and shear stress,^[60] we gain insights into two different scenarios at the GB: GB-like cavitation under tension/compression and GB migration under bending. FEM calculations were used to highlight the differences between the stress states during tension/compression versus bending.

4.1. FEM Calculations

An anisotropic crystal elastic/plastic model, implemented using the FEM with commercial code Abaqus, was used to analyze the ISs across the GB due to elastic anisotropy. The study considers both boundary conditions (tension/compression and bending) to investigate the potential driving force for GB migration under external loads. Prior to the extraction of the stresses in both crystals (**Figure 4**), the experimental stress–strain curve was first calibrated with this FEM-based crystal elastic/plastic model. The used elastic stiffness constants were $C_{11} = 168.4$ GPa, $C_{12} = 121.4$ GPa, and $C_{44} = 75.4$ GPa for Cu. Thus, the Zener’s anisotropy ratio for Cu is $A = 2C_{44}/(C_{11}-C_{12}) = 3.2$.

In **Figure 4**, the distribution of stress components (S_{22} , S_{33} , S_{12} , S_{13} , and S_{23}) across the GB is presented for both compression and bending. Based on these simulation results, a larger shear stress (S_{12}) exists parallel to the GB in the bending sample compared to the compression sample. The effect of the shear stress component, which is maximized at the GB and play important role on GB migration, will be addressed in Section 4.5. While the stress components (S_{12} , S_{22} , and S_{32}) are continuous across the GB due to traction vector continuity (considered as perfectly bonded), the other components show discontinuity.

4.2. SBs–GB Interactions in Cyclic Tension/Compression

To predict slip systems operating near the GB in bicrystals for uniaxial tension/compression, it is essential to consider elastic

Table 1. Summary results for the component crystals (CI and CII) for loading parallel to the GB: Schmid factors and normalized resolved shear stresses (RSSs) incorporating elastic incompatibility stresses (ISs) for the 12 conventional $\{111\}\langle 110 \rangle$ slip systems of perfect dislocations in fcc crystals (Cu). Highest values are plotted in bold.

Crystal Component	Crystal I		Crystal II	
	Schmid Factor	RSS/IS	Schmid Factor	RSS/IS
A2	0.11	0.11	0.21	0.14
A3	0.09	0.13	0.42	0.29
A6	0.21	0.24	0.20	0.14
B2	0.02	0.06	0.02	0.08
B4	0.13	0.12	0.06	0.01
B5	0.12	0.19	0.08	0.07
C1	0.35	0.37	0.14	0.15
C3	0.05	0.08	0.13	0.08
C5	0.40	0.46	0.27	0.25
D1	0.21	0.32	0.33	0.21
D4	0.28	0.34	0.49	0.39
D6	0.06	0.02	0.15	0.17

and plastic incompatibilities.^[62] In our analysis of slip activity, we evaluated our experimental results using an analytical model previously proposed in.^[62] This model considers the criteria based on the geometric relation, resolved shear stress (RSS) and ISs arising from misorientation and elastic anisotropy.^[63] Specifically, **Table 1** summarizes the results of the component crystals, CI and CII when loaded parallel to the GB. The Schmid factors and the RSSs are normalized by the applied stress, considering elastic ISSs. To calculate the RSS with the anisotropic model and ISSs, the cubic elastic moduli (C_{11} , C_{12} , and C_{44}) for Cu were used.

Table 2 summarizes the angles α and β (**Figure 4A**) as well as the geometric transmission factor (**TF**), for the boundary plane inclination of $\epsilon = 4^\circ$ measured experimentally. The angle α is the

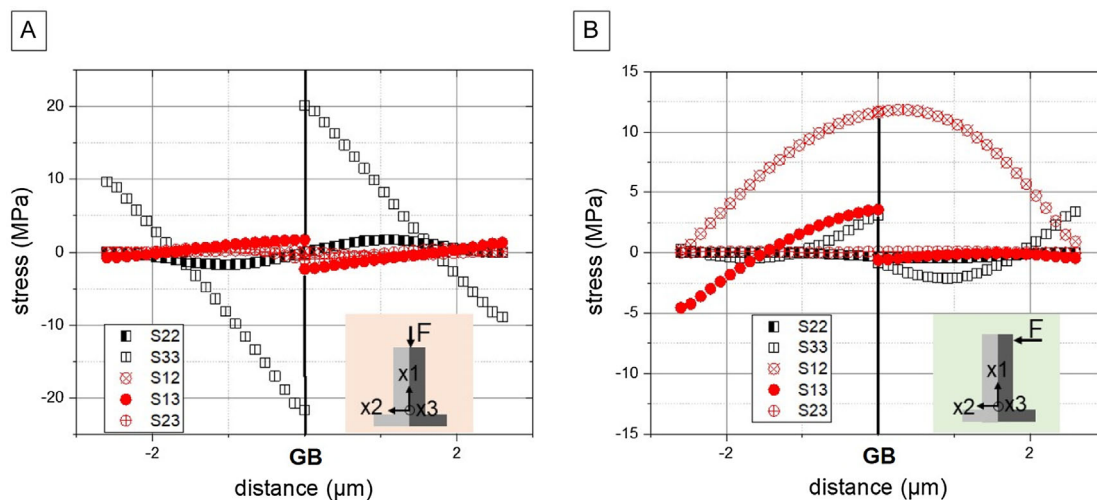


Figure 4. Variation of the stress tensor components across the GB of the bicrystal in A) compression and B) bending.

Table 2. Angles at the GB between primary slip system C5 in CI and the 12 slip systems in CII as well as the corresponding transmission factor (TF). Here, the Schmid–Boas notation is used for the definition of slip systems in fcc crystals, see appendix.

CI	C5											
CII	A2	A3	A6	B2	B4	B5	C1	C3	C5	D1	D4	D6
α		11				79		17			57	
β	42	39	88	42	81	26	83	39	26	83	81	88
TF	0.729	0.764	0.032	0.0141	0.029	0.171	0.117	0.742	0.859	0.066	0.083	0.017

angle formed by the intersection of slip planes of the two grains with the GB plane, β is the angle between the slip directions lying in the considered planes, and the TF shows 12 possible interactions when we assume single-slip deformation in CI (active slip system C5).

As CI plastically deformed by single slip, we analyzed the magnitude of residual Burgers vector b_{GB} for all 12 potentially active slip systems in CII (Figure 5). Figure 5B shows graphically the results of normalized b_{GB} for the 12 possible slip systems in CII. Here, as in Table 2, the slip systems of the outgoing dislocations are assumed to be in CII, and only C5 is considered in CI as the incoming dislocation slip system. The slip systems marked with arrows indicate the activated slip systems in CII, where 1SF, 2SF, and 4SF are the first, second, and fourth largest Schmid factors, respectively.

According to the results in Table 1 and 2, the SEM and AFM images in Figure 2 and 6, we identified the primary slip systems (C5 and D4) with the largest Schmid factor and normalized RSS in each component crystal. This means that C5 and D4 were most favorably inclined with respect to the loading axis. Figure 6A shows a simplified 3D schematic view of the slip planes–GB interaction for the active slip systems. The AFM images (Figure 6B) were incorporated for comparison. Figure 6A clarifies that the primary SBs mainly pile up at the GB, which is correlated with the quite large α angle and the low TF for the C5–D4 interaction, as shown in Table 2. Thus, there is pronounced slip incompatibility and stress concentrations close to the GB.

Figure 5 reveals that, despite the small TF (0.08) for the C5–D4 interaction, partial transmission likely occurs in terms of the magnitude of b_{GB} . This implies that as SBs repeatedly impinge on the GB, a substantial density of residual GBDs accumulates within the GB. Over successive loading cycles, these residual GBDs progressively hinder further slip, resulting in continuous increase in GB energy, consistent with findings in.^[52,61] During cycle deformation, ISs near the GB progressively increase with each cycle. This effect leads to the activation of secondary slip systems close to the GB. Notably, this effect was observed only in samples deformed under cyclic tension/compression, consistent with previous experimental results in uniaxial cyclic deformation.^[52,56] Furthermore, GB damages were mainly attributed to the PSBs impingement and showed correlation with the vertical component of the residual GBDs.^[52] An unexpected and intriguing experimental observation, challenging to explain based on Table 1 and 2 using Schmid factor and RSS, is the activation of C5 in CII during tension/compression. However, the angle α in Table 2 for the C5–A3 interaction is consistent with the condition for slip transmission, as proposed in.^[64]

4.3. SBs–GB Interactions in Cyclic Bending

Compared to the cyclic tension/compression, only primary SBs (C5 and D4) operated close to the GB in the samples subjected to cyclic bending. Meanwhile, the secondary slip system A3 within CII operated at the beams surface, where larger stresses exist, as

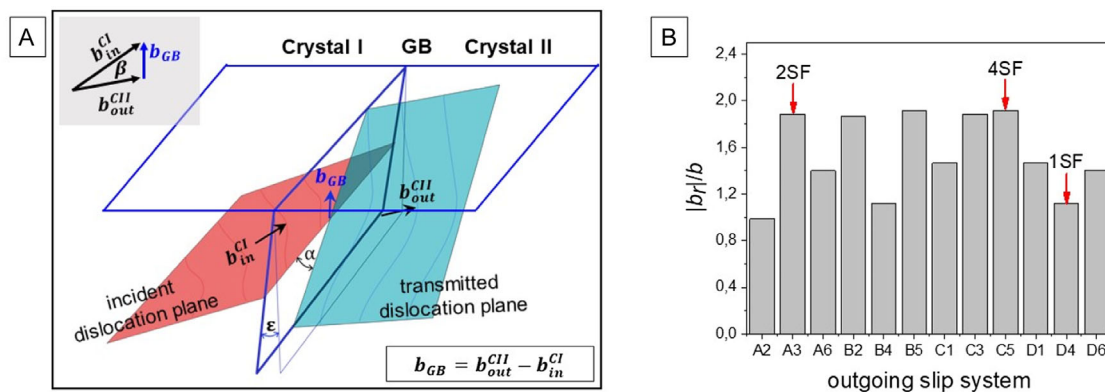


Figure 5. A) Schematic representation of the geometric slip transmission factor TF (with slip planes and slip directions) and the GB plane, where b_{in}^{CI} and b_{out}^{CII} are the Burgers vectors of the incident and transmitted dislocations, respectively. The difference between the b^{CI} and b^{CII} can be used to measure the magnitude of the residual GB dislocation b_{GB} left as debris in the interface during transmission. B) Magnitude of the residual Burgers vector b_{GB} associated with the 12 potentially active slip systems of the outgoing lattice dislocations in CII. The activated slip system of the outgoing lattice dislocations is indicated by the arrow 1SF (largest Schmid factor or RSS/IS for D4 slip system, see Table 1).

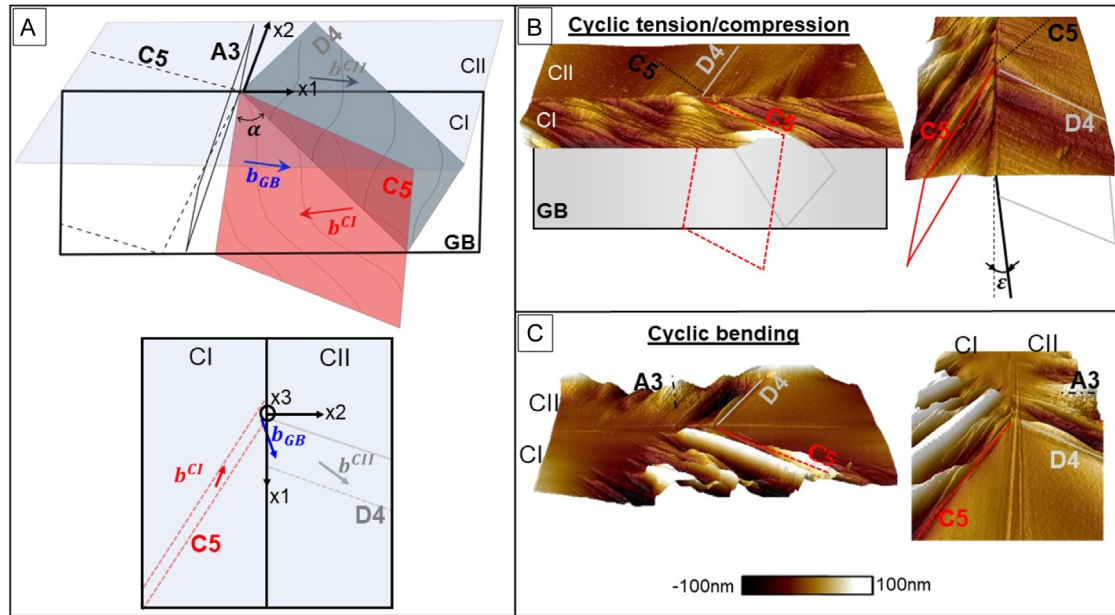


Figure 6. A) Simplified 3D and 2D overview of the slip planes–GB interaction shown in B and C. The 2D schematic picture depicts the slip planes associated with the incoming and outgoing dislocations within a crystal lattice (main slip systems).

shown in Figure 6C. Additionally, the results showed that the GB migrates during cyclic bending. This observation highlights the significant effect of existing shear stresses induced by bending (see Figure 4B) as the driving force for GB migration. This finding aligns with existing literature on the topic.^[10,19,22,27–30,65] At the atomic scale, disconnections are mainly responsible for a progressive normal displacement of the GB due to shear-coupled GB migration.^[28–30] Stepwise GB migration is related to the step height and to the Burgers vector direction of disconnections accompanying shear deformation. According to Cahn's geometrical model,^[10,66] the coupling characteristics of HAGB and LAGB can be also expressed by this geometric theory, despite their limitations in terms of predicting disconnection properties (including coupling factor). However, identifying disconnections with the smallest magnitudes of step height vectors and/or Burgers vectors that yield the lowest critical RSS can reasonably serve as reasonable candidates for the actual step vector.^[10,66] Therefore, our discussion on shear-coupled GB migration will be based on the assumption that the disconnections (GBDs) within the GB are perfect disconnections with the smallest step vector. It is crucial to highlight that investigating the GB structure through experimental evidence can provide valuable insights into key features related to disconnections, such as step height and Burgers vector direction.^[26] Due to the challenges associated with experimentally characterizing the GB structure of an incoherent HAGB, we have followed Cahn's work^[10] and made the aforementioned assumptions for discussing our results.

As mentioned earlier, other GB migration mechanisms (as in the context of recrystallization) can also be driven by other forces, such as capillarity forces,^[8] anisotropy of elastic constants, and free surfaces.^[44,51] Additionally, Peach–Koehler (PK) forces^[19,44,65] and the GB energy, which includes elastic stored energy arising from dislocations,^[44,67] play significant roles. In

general, a GB will move if a free energy jump exists between adjacent grains.^[26,44] In conventional monotonic loading deformations,^[22] shear-coupled GB migration can be often quantified using Cahn's model through the coupling factor, which is the ratio between tangential and normal displacements during a GB migration event.^[10] In cyclic deformation experiments, quantification of GB migration by the coupling factor is critical, as highlighted by Wang et al.^[27] MD simulations also revealed that disconnection-mediated GB migration is reversible under cyclic shear deformations.^[27] Recently, similar results were observed in gold (Au) bicrystals with $\Sigma 11(113)$ coherent GB using an in situ testing technique and MD simulations.^[30] Related to cyclic loading, the GB migrates downward and upward. On average, the GB showed a stagnation state.^[30] However, our experimental findings during cyclic bending show that GB migration preferentially occurs in the negative x_2 -direction (toward CI). This directional preference suggests that CI is irreversibly consumed during cyclic loading in the experiment, indicating the influence of an additional driving force on GB migration. Recently, Richeton et al.^[51] conducted numerical simulations demonstrating that crystallographic misorientation and elastic anisotropy play a significant role in the variation of the stored energy during GB migration. To gain deeper insights into the microscopic deformation mechanisms underlying our experimental observations, we performed analytical and numerical analysis of the elastic ISs, image stresses arising from elastic anisotropy, and PK driving force. These analyses were based on the theoretical calculations reported in.^[51,54,68]

4.4. Analysis of Dislocation Image Stress Effects

Generally, dislocations in the vicinity of GBs are subjected to several type of forces, such as the interfacial intrinsic stress field,

applied stress field, and ISs. Due to the different elastic anisotropic properties of component crystals, a dislocation also experiences an additional image force produced by the interface. This is because the total elastic self-energy of a dislocation varies with its position relative to the interface.^[1] This image force (or self-force) is evaluated by the PK equation.^[1,69] Therefore, in our study, we employed the recent theoretical derivations proposed by Chen et al.^[68] to simulate an anisotropic bicrystal with free surfaces and a perfectly bounded planar GB oriented with its normal along the x_2 -direction (as depicted in **Figure 7A**). The specific equation details required for the calculations were reported by Chen et al.^[68]

In this model, an edge dislocation was considered, located at the (X_1, X_2) position for the slip system with the highest Schmid factor. The dislocation line vector \mathbf{t} is supposed to be along the X_3 -direction. In **Figure 7A**, the Burgers vector \mathbf{b} of the dislocation lying on the D4 slip system in CII points toward the GB and the angle φ was taken from experimental results ($\varphi_I = 24^\circ$, $\varphi_{II} = 63^\circ$).

The results in **Figure 7B** show that the projected resolved image stress τ_{im} (projected image force divided by the $|\mathbf{b}|$) of Cu along the slip direction in CI and CII for bicrystals with sizes w ranging from 1 to 6 μm .

Positive image stress τ_{im} indicates that the GB attracts dislocations. Conversely, in the case of negative τ_{im} , a dislocation is repelled by the GB or free surface. **Figure 7** clearly shows the impact of crystal orientation and finite size effects on image

stress, consistent with recent calculations.^[51,68] When the dislocation lies in CI on the C5 slip system and approaches the GB, the image stress acting on the dislocation rapidly increases at ≈ 0.1 (≈ 100 nm away from the GB). This increased image stress attracts the dislocation toward the GB. Conversely, a dislocation in CII on D4 experiences repulsion from the GB as it nears the GB. **Figure 7B** also demonstrates the effect of finite size effects (inherent to the distance to free surface) on dislocation image stresses. For example, a dislocation within CI with $w = 1 \mu\text{m}$ rapidly experiences surface image forces approximately at 100 nm (0.1) away from the GB. However, for larger bicrystals ($w > 4 \mu\text{m}$), this effect is less pronounced. Notably, the effect of the free surface extends over a longer distance compared to the GB effect (or misorientation effect). In CII, the free surface image stress effect contributes to an additional repulsion between dislocations and the GB. Consequently, dislocations in CII are more readily repelled at the GB, especially in very small samples where surface image stresses are more pronounced (e.g., in the case of the 1 μm -sized bicrystal).

Based on the previously numerical results and subsequent discussion, it can be inferred that distinct dislocation densities may accumulate between CI and CII near the GB due to variation in image stresses for lattice dislocations. This phenomenon may result in an elastic energy jump creating a driving force near the GB. This energy driving force is independent of the loading condition. This implies that such a driving force should be present in both test samples, whether they are

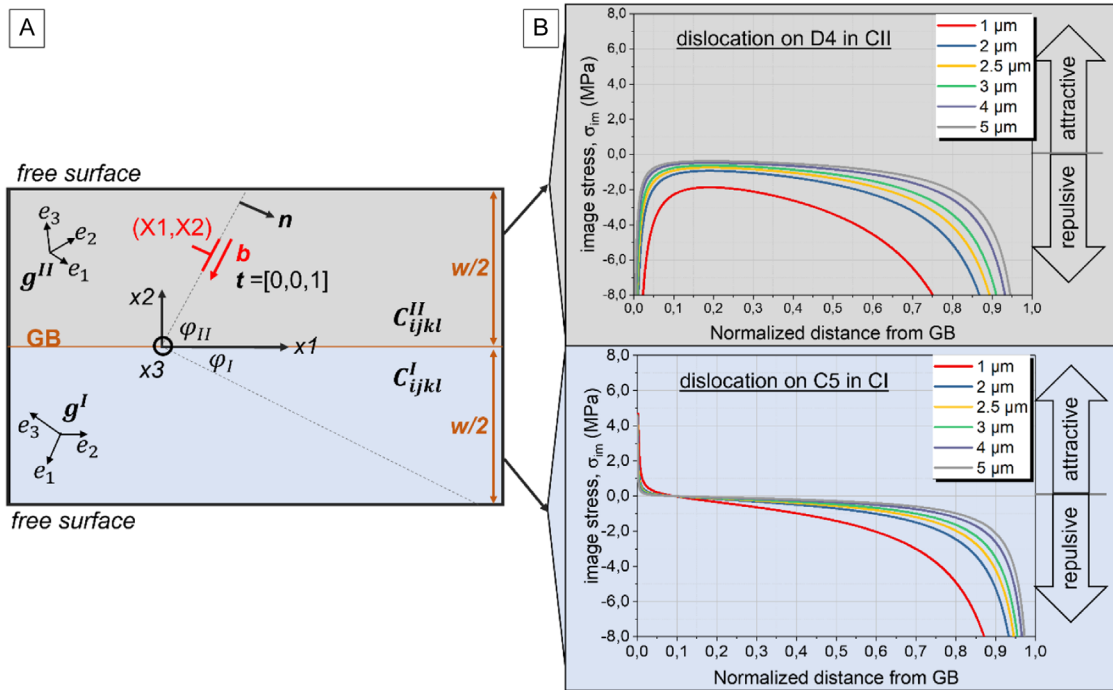


Figure 7. Bicrystal configuration with one single edge dislocation in CII (as an example), with different crystallographic orientations ($\mathbf{g}^I, \mathbf{g}^{II}$) of the component crystals and with anisotropic elastic properties described by respective elastic stiffness tensors ($C^I_{ijkl}, C^{II}_{ijkl}$) A); variation of the projected image stress τ_{im} in CI and CII with the distance from the GB along the slip direction normalized by $w/2$ for bicrystals with sizes between 1 and 6 μm . Negative image stress τ_{im} leads to a repulsive on the dislocation, while positive τ_{im} leads to attractive effect B).

deformed under tension/compression or bending. The fact that GB migration occurs exclusively under cyclic bending suggest that the GB is not solely driven by free energy jump-driving force. Instead, shear-coupled GB migration likely plays a role, especially considering the important shear stress at GB during bending (see Figure 4B).

4.5. Coupling of Shear Stress and Elastic Energy Jump-Driving Forces to GB Migration

Shear-coupled GB migration occurs through the glissile motion of disconnections. According to Cahn's model^[10] and as described earlier in Section 4.3, these disconnections are often associated with steps following appropriate vectors of the DSC (displacement shift complete) lattice. Despite the limitations of this geometric analysis, this shear coupling mechanism is highly sensitive to external applied stress and

temperature.^[10,22,29,30] Intrinsic disconnections, which play a major role in disconnection-mediated GB migration, are well-known features within GBs.^[29,70] However, it is important to note that disconnections can also arise from the interactions between lattice dislocations and GB, as described by Rajabzadeh et al.^[29] and Hirth et al.^[34] In the context of dislocations interaction with GBs, it is observed that the Burgers vector of an impinging lattice dislocation can undergo dissociation. This phenomenon occurs to accommodate the stress within the GB itself. Specifically, the dissociation results in two types of GBDs: glissile GBDs (with the Burgers vector parallel to the GB plane, denoted as b_{\parallel}) and sessile GBDs (with the Burgers vector perpendicular to the GB plane, denoted as b_{\perp})^[1,26] (considering the conservation of the total Burgers vector). **Figure 8A** visually depicts this lattice dislocation–GB interaction, highlighting the components of the residual Burgers vector, both normal and parallel to the GB plane. Above a critical stress, shear-coupled GB migration

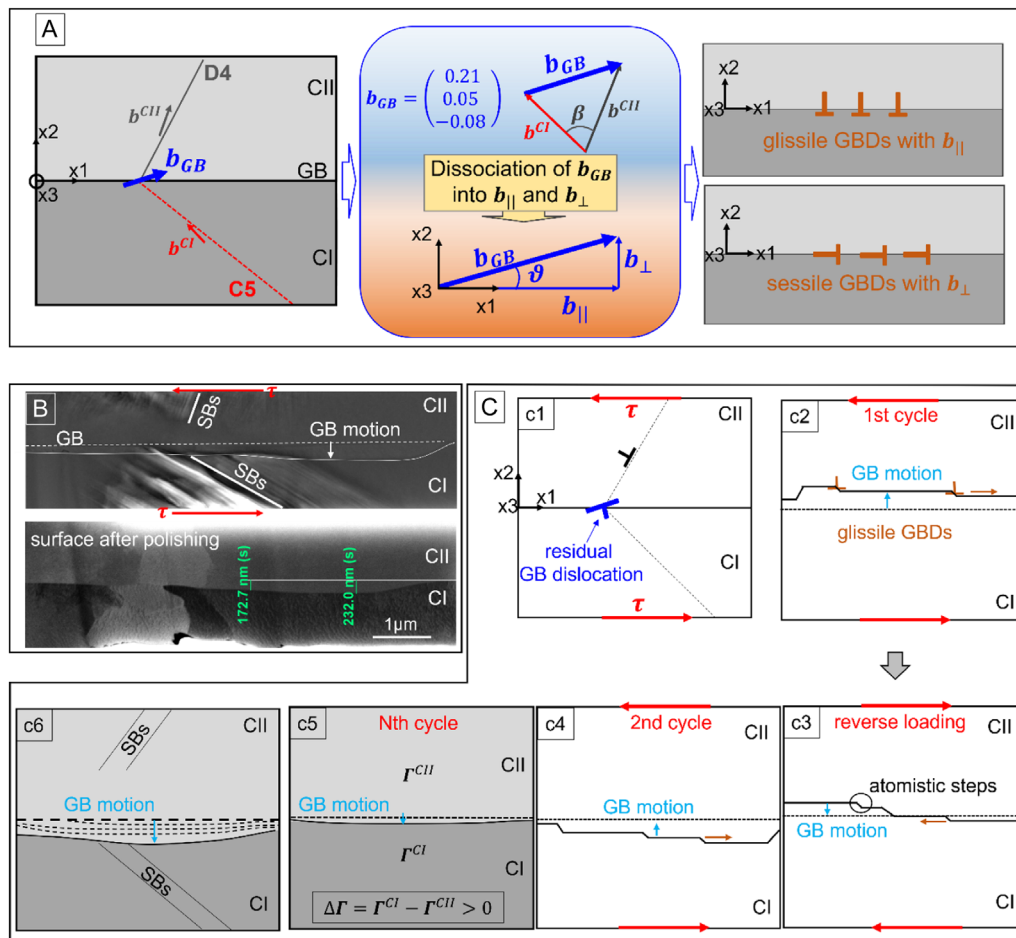


Figure 8. Schematic representation of shear-coupled GB migration due to creation and motion of disconnections (GBDs). A) Illustration of the primary slip systems on both sides of the GB and vector resolution of a residual grain boundary dislocation with the Burgers vector b_{GB} and its dissociation into GBDs with the Burgers vectors b_{\parallel} and b_{\perp} . B) SEM image of discontinuous SBs–GB interaction and surface after polishing. C) Disconnection-mediated GB migration based on.^[26–28,30] c1) Illustration of an indirect transmission of a lattice dislocation and creation of a residual GB dislocation. c2) During the first cycle: local GB migration by lateral motion of atomistic steps (after dissociation of residual GB dislocations in glissile/sessile disconnections with the height of one or two atomic layers). c3) During reverse loading, the GB moves downward. c4) The GB migrates both upward and downward. c5) GB migration in the negative x_2 -direction (toward CI) due to the driving force $\Delta\Gamma$. c6) Final GB migration after 10^4 cycles as in Figure 8B.

can occur due to the lateral motion of layer-by-layer glissile GBDs.^[28,31,70] For instance, in pristine GBs with a misorientation of 25°, the critical stress to induced shear-coupled GB migration is around 50 MPa. However, in GBs with preexisting disconnections, the critical stress is significantly lower, being less than 5 MPa.^[70] Consequently, the existing shear stresses induced by cyclic bending are sufficiently high to move the GB forward by the glide motion of glissile GBDs. In contrast, sessile GBDs require climb for displacement and substantial stresses to further dissociate into glissile GBDs.^[29,70] This specific topic on sessile GBDs will not be discussed further in this context. For consistency, we will use the term “GBDs” exclusively to refer to sessile GBDs/disconnections in the following.

To gain insight into the microscopic GB migration mechanisms in our experiments (as depicted in Figure 8B), the total driving force (f_{GB}) is important to derive the equation of motion for GBs.^[14,26,71] This driving force is first linked to the externally applied shear stress and, consequently, to the Burgers vector of GBDs $b_{glissile}$ through, for example, the PK force f_{τ} . Additionally, another component, denoted as f_h , is associated with the elastic energy jump-driving force across the GB. This force couples to the height of the shear coupling process. Related to our previous discussion, f_h can arise from several sources, including elastic anisotropy, dislocation density inhomogeneity, or capillary force. Our analytical and numerical investigations consistently revealed the presence of an elastic energy jump-driving force within our bicrystal which is attributed to elastic anisotropy and image stress effects.

In previous studies,^[27,30] researchers have observed that GB migration is fully reversible during loading cycles. However, our experimental findings during cyclic bending contradict this observation. Upon further analysis, it becomes evident that both driving forces ($f_{GB} = f_{\tau} + f_h$) play an essential role in GB migration. Specifically, f_{τ} couples to the intrinsic and extrinsic GBDs, governing their lateral motion at the atomistic scale, while f_h determines the GB motion direction. These combined forces explain our experimental observation of shear-coupled GB migration during cyclic bending, even though the exact description of preexisting disconnections (i.e., intrinsic GB defects) remains unknown in this schematic picture.

Based on our experimental observations, analytical/numerical studies, and insights from previous studies,^[26,27,29,30,70] we present a schematic representation of shear-coupled GB migration based on an analysis of GBDs during cyclic bending (Figure 8B,C). To achieve this representation, we make the following assumptions: glissile GBDs form at the GB during the glide transfer mechanism. Additionally, the motion of GBDs remains unaffected by the glide transfer, which is consistent with findings reported by Zhu et al.^[72] After the dissociation of the residual grain boundary dislocations (GBDs) (c1) into sessile and glissile GBDs during the initial loading, the existing shear stresses parallel to the GB activate lateral motion of the GBDs with the smallest step vector (intrinsic GBDs, which are unknown, are not considered in the schematic picture). This process results in upward GB migration (c2). Similarly, when the sample is loaded in the opposite direction, the GB moves

downward (c3). During subsequent loading cycles, the GB migrates both upward and downward (c4) through the motion of GBDs in a layer-by-layer fashion, revealing a reversible behavior. The preferential migration of the GB in the negative x_2 -direction (toward CI), as observed in our experiments, is likely enhanced by the existing elastic energy jump-driving force (denoted as $\Delta\Gamma$ in Figure 8C). This force is coupled to the height of the shear-coupled GB migration process. The energy jump-driving force, as previously discussed, can arise from various sources. Our previous analytical analysis (see Figure 7) indicates that this energy jump-driving force, resulting from elastic anisotropy in copper, could also lead to a difference in dislocation density near the GB between CI and CII. This difference in dislocation density accumulates after N cycles (c4), resulting in a driving force (f_h) that determine the direction of irreversible GB migration (c5). This scenario aligns well with our experimental observations (see Figure 8B). Another plausible scenario could be related to the diverse DSC Burgers vectors. These systems offer numerous potential combinations for GBDs steps. For instance, when an external load is applied in a specific direction, it is highly probable that the shear stress only acts on a family of GBDs because they are mobile. Conversely, during load reversal, other GBDs that require higher stresses or spread core may dominate. Therefore, shear-coupled GB migration takes place in a preferred direction during cyclic loading.

5. Conclusions

In the present study, copper micro-bicrystals with a specific HAGB and an average size of 2–6 μm were subjected to cyclic deformation using two different loading conditions: cyclic tension/compression and cyclic bending. The experiments were conducted in situ within a SEM at room temperature. Additionally, this experimental investigation was complemented by analytical and numerical simulations. The following results were obtained: 1) We employed an analytical model to analyze slip activity in our experimental results. This model accounts for geometric relations, RSS, and ISs arising from misorientation and elastic anisotropy. 2) Based on the outcomes, we identified the primary slip systems with the largest Schmid factor and normalized RSS in each component crystal (C5 and D4). 3) In cyclic tension/compression experiments, GB damage was attributed to impinging primary SBs and the vertical component of residual GBDs. 4) Bicrystals exhibited a GB migration, primarily in the negative x_2 -direction, as compared to cyclic tension/compression experiments. 5) We explained this process as a shear-coupled GB migration, which is based on disconnection motion. 6) The preferential migration toward CI (in the negative x_2 -direction) observed in our experiments may be influenced by the existing elastic energy jump-driving force, coupled to the height of disconnections which is inherent to shear-coupled GB migration. Additionally, the role of non-glissile GBDs has been considered in this context, during the reverse loading.

Appendix

Table A.1. The 12 slip systems in the fcc crystallographic structure with Schmid and Boas's notation.^[7,3]

Notation	Crystallographic plane	Crystallographic direction
A2	$(\bar{1} 1 1)$	$[0 \bar{1} 1]$
A3	$(\bar{1} 1 1)$	$[1 0 1]$
A6	$(\bar{1} 1 1)$	$[1 1 0]$
B2	$(1 1 1)$	$[0 \bar{1} 1]$
B4	$(1 1 1)$	$[\bar{1} 0 1]$
B5	$(1 1 1)$	$[\bar{1} 1 0]$
C1	$(\bar{1} \bar{1} 1)$	$[0 1 1]$
C3	$(\bar{1} \bar{1} 1)$	$[1 0 1]$
C5	$(\bar{1} \bar{1} 1)$	$[\bar{1} 1 0]$
D1	$(1 \bar{1} 1)$	$[0 1 1]$
D4	$(1 \bar{1} 1)$	$[\bar{1} 0 1]$
D6	$(1 \bar{1} 1)$	$[1 1 0]$

Acknowledgements

The authors would like to thank the Deutsche Forschungsgemeinschaft (DFG) (MO2672/2-1) for the economic resources that have helped carry out this project, as well as for the financing of the microscopes (SEM and AFM) (grant no. INST 256/455-1FUGG) of great relevance for this type of research. The authors would also like to thank B. Nothdurft, D. Zimmermann, L. Schon, and M. Zamanzade for their experimental assistance in the FIB and AFM, as well as the group *physical analytic* from INM-Leibniz Institute für neue Materialien for the FIB.

Open Access funding enabled and organized by Projekt DEAL.

Conflict of Interest

The authors declare no conflict of interest.

Data Availability Statement

The data that support the findings of this study are available from the corresponding author upon reasonable request.

Keywords

disconnections, dislocation pile-ups, energy jump-driving force, fatigue, grain boundary migration, micro-bicrystal

Received: February 16, 2024

Revised: June 20, 2024

Published online: July 11, 2024

- [1] A. P. Sutton, R. W. Balluffi, *Interfaces in Crystalline Materials*, Clarendon Press, Oxford **1996**.
 [2] S. Suresh, *Fatigue of Materials*, Cambridge University Press, Cambridge **1998**.
 [3] H. Vehoff, A. Nykyforchyn, R. Metz, *Mater. Sci. Eng. A* **2004**, 387–389, 546.

- [4] Q. Yu, M. Legros, A. M. Minor, *MRS Bull.* **2015**, 40, 62.
 [5] K. Zhang, J. R. Weertman, J. A. Eastman, *Appl. Phys. Lett.* **2005**, 87, 1.
 [6] D. S. Gianola, S. Van Petegem, M. Legros, S. Brandstetter, H. Van Swygenhoven, K. J. Hemker, *Acta Mater.* **2006**, 54, 2253.
 [7] T. J. Rupert, D. S. Gianola, Y. Gan, K. J. Hemker, *Science* **2009**, 326, 1686.
 [8] F. Mompou, D. Caillard, M. Legros, *Acta Mater.* **2009**, 57, 2198.
 [9] J. W. Cahn, J. E. Taylor, *Acta Mater.* **2004**, 52, 4887.
 [10] J. W. Cahn, Y. Mishin, A. Suzuki, *Acta Mater.* **2006**, 54, 4953.
 [11] S. Berbenni, B. Paliwal, M. Cherkaoui, *Int. J. Plast.* **2013**, 44, 68.
 [12] M. Winning, G. Gottstein, L. S. Shvindlerman, *Mater. Sci. Eng. A* **2001**, 317, 17.
 [13] M. Winning, *Acta Mater.* **2003**, 51, 6465.
 [14] T. Gorkaya, T. Bulet, D. A. Molodov, G. Gottstein, *Scr. Mater.* **2010**, 63, 633.
 [15] D. A. Molodov, *Diffus. Found.* **2015**, 5, 247.
 [16] C. H. Li, E. H. Edwards, J. Washburn, E. R. Parker, *Acta Metall.* **1953**, 1, 223.
 [17] W. T. Read, W. Shockley, *Phys. Rev.* **1950**, 78, 275.
 [18] M. Biscondi, C. Goux, *Mem. Sci. Rev. Met.* **1968**, 65, 167.
 [19] M. Winning, G. Gottstein, L. S. Shvindlerman, *Acta Mater.* **2001**, 49, 211.
 [20] M. Winning, G. Gottstein, L. S. Shvindlerman, *Acta Mater.* **2002**, 22, 353.
 [21] D. A. Molodov, V. A. Ivanov, G. Gottstein, *Acta Mater.* **2007**, 55, 1843.
 [22] T. Gorkaya, D. A. Molodov, G. Gottstein, *Acta Mater.* **2009**, 57, 5396.
 [23] D. A. Molodov, T. Gorkaya, G. Gottstein, *J. Mater. Sci.* **2011**, 46, 4318.
 [24] N. Combe, F. Mompou, M. Legros, *Phys. Rev. B* **2016**, 93, 1.
 [25] A. Rajabzadeh, F. Mompou, M. Legros, N. Combe, *Phys. Rev. Lett.* **2013**, 110, 1.
 [26] J. Han, S. L. Thomas, D. J. Srolovitz, *Prog. Mater. Sci.* **2018**, 98, 386.
 [27] P. Wang, X. Yang, D. Peng, *Metall. Mater. Trans. A: Phys. Metall. Mater. Sci.* **2017**, 48, 4977.
 [28] A. Rajabzadeh, M. Legros, N. Combe, F. Mompou, D. A. Molodov, *Philos. Mag.* **2013**, 93, 1299.
 [29] A. Rajabzadeh, F. Mompou, S. Lartigue-Korinek, N. Combe, M. Legros, D. A. Molodov, *Acta Mater.* **2014**, 77, 223.
 [30] Q. Zhu, G. Cao, J. Wang, C. Deng, J. Li, Z. Zhang, S. X. Mao, *Nat. Commun.* **2019**, 10, 1.
 [31] M. F. Ashby, *Surf. Sci.* **1972**, 31, 498.
 [32] J. P. Hirth, R. W. Balluffi, *Acta Metall.* **1973**, 21, 929.
 [33] J. P. Hirth, *J. Phys. Chem. Solids* **1994**, 55, 985.
 [34] J. P. Hirth, R. C. Pond, J. Lothe, *Acta Mater.* **2006**, 54, 4237.
 [35] M. W. Kapp, O. Renk, T. Leitner, P. Ghosh, B. Yang, R. Pippan, *J. Mater. Res.* **2017**, 32, 4317.
 [36] H. Mughrabi, H. W. Höppel, M. Kautz, *Scr. Mater.* **2004**, 51, 807.
 [37] M. W. Kapp, T. Kremmer, C. Motz, B. Yang, R. Pippan, *Acta Mater.* **2017**, 125, 351.
 [38] O. Renk, A. Hohenwarter, R. Pippan, *Adv. Eng. Mater.* **2012**, 14, 948.
 [39] M. Legros, D. S. Gianola, K. J. Hemker, *Acta Mater.* **2008**, 56, 3380.
 [40] M. Jin, A. M. Minor, J. W. Morris, *Thin Solid Films* **2007**, 515, 3202.
 [41] S. Brandstetter, K. Zhang, A. Escudero, J. R. Weertman, H. Van Swygenhoven, *Scr. Mater.* **2008**, 58, 61.
 [42] K. Kashihara, F. Inoko, *Acta Mater.* **2001**, 49, 3051.
 [43] M. P. Dewald, W. A. Curtin, *Model. Simul. Mater. Sci. Eng.* **2007**, 15, S193.
 [44] G. Gottstein, L. S. Shvindlerman, *Grain Boundary Migration in Metals: Thermodynamics, Kinetics, Applications, Second Ed.*, CRC Press, Boca Raton **2009**.
 [45] D. Kiener, W. Grosinger, G. Dehm, R. Pippan, *Acta Mater.* **2008**, 56, 580.
 [46] Y. Cui, Z. Liu, Z. Wang, Z. Zhuang, *J. Mech. Phys. Solids* **2016**, 89, 1.

- [47] T. Sumigawa, K. Byungwoon, Y. Mizuno, T. Morimura, T. Kitamura, *Acta Mater.* **2018**, *153*, 270.
- [48] D. Kiener, C. Motz, W. Grosinger, D. Weygand, R. Pippan, *Scr. Mater.* **2010**, *63*, 500.
- [49] J. Rafael Velayarce, C. Motz, *Materials* **2020**, *13*, 741.
- [50] N. Kheradmand, A. F. Knorr, M. Marx, Y. Deng, *Acta Mater.* **2016**, *106*, 219.
- [51] T. Richeton, X. Chen, S. Berbenni, X. Chen, *Philos. Mag.* **2020**, *0*, 1.
- [52] L. L. Li, P. Zhang, Z. J. Zhang, Z. F. Zhang, *Acta Mater.* **2013**, *61*, 425.
- [53] J. P. Liebig, S. Krauß, M. Göken, B. Merle, *Acta Mater.* **2018**, *154*, 261.
- [54] X. Chen, T. Richeton, C. Motz, S. Berbenni, *Crystals* **2020**, *10*, 411.
- [55] J. Nellessen, S. Sandlöbes, D. Raabe, *Mater. Sci. Eng. A* **2016**, *668*, 166.
- [56] W. Liu, M. Bayerlein, H. Mughrabi, A. Day, P. N. Quested, *Acta Metall. Mater.* **1992**, *40*, 1763.
- [57] L. C. Lim, R. Raj, *Acta Metall.* **1985**, *33*, 2205.
- [58] M. D. Sangid, H. J. Maier, H. Sehitoglu, *Int. J. Plast.* **2011**, *27*, 801.
- [59] Z. F. Zhang, Z. G. Wang, *Philos. Mag. Lett.* **2000**, *80*, 483.
- [60] E. Bayerschen, A. T. McBride, B. D. Reddy, T. Böhlke, *J. Mater. Sci.* **2016**, *51*, 2243.
- [61] M. D. Sangid, T. Ezaz, H. Sehitoglu, *Mater. Sci. Eng. A* **2012**, *542*, 21.
- [62] I. Tiba, T. Richeton, C. Motz, H. Vehoff, S. Berbenni, *Acta Mater.* **2015**, *83*, 227.
- [63] T. Richeton, S. Berbenni, *Eur. J. Mech. - A/Solids* **2013**, *37*, 231.
- [64] E. Werner, W. Prantl, *Acta Met. Mater.* **1990**, *38*, 533.
- [65] T. Gorkaya, K. D. Molodov, D. A. Molodov, G. Gottstein, *Acta Mater.* **2011**, *59*, 5674.
- [66] J. W. Cahn, Y. Mishin, A. Suzuki, *Philos. Mag.* **2006**, *86*, 3965.
- [67] M. Winning, *Scr. Mater.* **2008**, *58*, 85.
- [68] X. Chen, T. Richeton, C. Motz, S. Berbenni, *Int. J. Plast.* **2021**, *142*, 102967.
- [69] P. M. Anderson, J. P. Hirth, J. Lothe, *Theory of Dislocations*, 3rd ed. Cambridge University Press, Cambridge **2017**.
- [70] H. A. Khater, A. Serra, R. C. Pond, J. P. Hirth, *Acta Mater.* **2012**, *60*, 2007.
- [71] K. Chen, J. Han, X. Pan, D. J. Srolovitz, *Proc. Natl. Acad. Sci. U. S. A.* **2020**, *117*, 4533.
- [72] Q. Zhu, S. C. Zhao, C. Deng, X. H. An, K. X. Song, S. X. Mao, J. W. Wang, *Acta Mater.* **2020**, *199*, 42.
- [73] E. Schmid, W. Boas, *Plasticity of Crystals with Special Reference to Metals*, Chapman & Hall, London **1968**.